Effect of elastic instability on mobilization of capillary entrapments

Cite as: Phys. Fluids **33**, 113102 (2021); https://doi.org/10.1063/5.0071556
Submitted: 15 September 2021 • Accepted: 20 October 2021 • Published Online: 03 November 2021

Pegah Shakeri, Michael Jung and Ralf Seemann

Physics of Fluids ARTICLE scitation.org/journal/phf

Effect of elastic instability on mobilization of capillary entrapments

Cite as: Phys. Fluids **33**, 113102 (2021); doi: 10.1063/5.0071556
Submitted: 15 September 2021 · Accepted: 20 October 2021 ·
Published Online: 3 November 2021

Pegah Shakeri,[1,2,a)] Michael Jung,[1,2,b)] and Ralf Seemann[1,2]

AFFILIATIONS

[1]Experimental Physics, Saarland University, 66123 Saarbrücken, Germany
[2]Max Planck Institute for Dynamics and Self-Organization, 37077 Göttingen, Germany

[a)]Author to whom correspondence should be addressed: pegah.shakeri@physik.uni-saarland.de
[b)]michael.jung@physik.uni-saarland.de

ABSTRACT

The flow of viscoelastic polymer solutions and their use as displacing agents in porous media are important for industrial applications, such as enhanced oil recovery and soil remediation. The complexity of flow and high elasticity of conventionally used viscoelastic polymer solutions can lead to purely elastic instability in porous media. In this study, we investigate the impact of this instability on displacing capillary entrapments at low Reynolds numbers using a microfluidic approach. Our unique design consists of a single-capillary entrapment connected to two symmetric serpentine channels. This design excludes the effect of viscous forces and enables a direct focus on displacement processes driven solely by elastic forces. After the onset of purely elastic instability, an unstable base flow is observed in the serpentine channels. We discuss that the pressure fluctuations caused by this unstable flow create an instantaneous non-equilibrium state between the two ends of the capillary entrapment. This provides the driving pressure to overcome the capillary threshold pressure and eventually displace the entrapped oil. In our geometry, we observe that the displacement coincides with the emergence of a fully developed elastic turbulent state.

I. INTRODUCTION

The addition of high molecular weight polymers to a Newtonian solvent results in a viscoelastic fluid, i.e., a fluid with intermediate mechanical properties between viscous fluids and elastic solids. Large elastic stresses induced during the flow of viscoelastic fluids lead to purely elastic instability even in the absence of inertia, i.e., at low Reynolds numbers.[1,2] As the polymers approach their maximum capacity for alignment with the flow and reach a so-called stretched state, they exert a significant back reaction to the flow above a critical shear rate, $\dot{\gamma}_{crit}$.[3] In other words, purely elastic instability occurs when the polymer relaxation time exceeds its transit time and elastic stresses are no longer fully dissipated.[4] The excessive elastic stresses elicit an unstable base flow. This unstable flow resembles inertia-induced hydrodynamic turbulent flow below the dissipation scale (Kolmogorov length), which is known as the "Batchelor regime."[5,6] This regime is characterized by spatially smooth, temporary random instabilities that cover a wide range of frequencies.[5,7,8] This is reflected as a power-law decay $\sim f^{-\beta}$ of the power spectral density (PSD) of kinetic energy with a characteristic exponent $\beta > 3$.[2,7,9–13] The occurrence of purely elastic instability during the flow of viscoelastic fluids in various geometries has been extensively studied in the literature.[2,7,14–17] Elastic instability is known to improve the efficiency of heat transfer[18–22] and microfluidic mixing.[23–26] Recently, it has been observed in enhancement oil recovery that purely elastic instability might play a crucial role in capillary entrapments (ganglia) displacement in porous media.[27–29]

Several experimental and numerical studies have focused on basic designs to study the microscopic behavior of viscoelastic fluids and elastic instability in porous media. A few basic geometries are commonly considered to mimic porous media flow characteristics at the microscale including straight channels embedded with uniform or randomized post arrays;[30–40] a single pore formed by four disks;[41,42] and converging and diverging channels.[43–45] All of these geometries have a curved streamline component in common. In fact, the streamline curvature of viscoelastic fluid flows can amplify the normal stress differences that lead to unstable flow.[17,46–48]

Purely elastic instability in porous media is commonly associated with increased flow resistance, i.e., an increased apparent viscosity even at low Reynolds numbers.[7,14,49–52] However, this increased apparent viscosity is not *per se* large enough to explain the improved

displacement efficiency of capillary entrapments in porous media. Displacement experiments performed using polymers with different molecular weights suggest that the mobilization of capillary entrapments is in fact caused by the unstable nature of flow.[27,49,53] The unstable flow induces fluctuations of the fluid–fluid interface in between the viscoelastic invading fluid and the trapped oil ganglia.[53–56] These fluctuations can lead to breakup of large ganglia into smaller droplets and eventually complete removal of the trapped defending phase.[57]

In this study, we use a microfluidic approach to investigate the mechanism by which a single-capillary entrapment is displaced by viscoelastic polymer solutions in the semi-dilute regime. We use serpentine channels with constant cross section to mimic the shear-dominated, curved (tortuous) nature of flow in porous media. We focus on the underlying elasticity-induced phenomena to establish a link with the displacement of capillary entrapment. To exclude inertial effects and evaluate the observations as purely elasticity-induced effects, we conduct microfluidic experiments at small Reynolds numbers $Re < \mathcal{O}(10^0)$ in the creeping flow regime. This paper is structured as follows: the methods utilized including the experimental setup, sample preparation, and fundamentals of the relevant fluid model are described in Sec. II; in Sec. III, we provide rheological characterizations of the polymer solutions and present and discuss the results of the microfluidic experiments; and we conclude the paper in Sec. IV.

II. METHODS

A. Microfluidic geometry

The microfluidic geometry employed in this work consisted of two identical serpentine channels of width $w_{mc} = 0.125$ mm that were connected by a perpendicular side channel of width $w_{sc} = 0.05$ mm and length $l_{sc} = 1$ mm [Fig. 1(a)]. The inner and outer radii of curvature of the serpentine channels were $r_i = 0.125$ mm and $r_o = 0.25$ mm, respectively. The height h of the microfluidic channels was approximately 0.045 mm. Serpentine channels were ideally suited for mimicking tortuous flow in porous media, whereas the perpendicular side channel provided the possibility of capillary entrapment of the oil phase. This geometry resembled a capillary entrapment between two grains, where fluid interfaces are in contact with more than one active pathway of the invading phase [Fig. 1(b)]. Together with a common inlet and outlet, the symmetry of serpentine channels provided an equal viscous pressure at both ends of the side channel. Hence, our microfluidic geometry served as a model system that isolated the effect of elastic stresses on the fluid–fluid interfaces and consequently on the mechanism of oil displacement from the side channel.

B. Experimental protocol

The microfluidic devices were fabricated following a standard soft-lithographic procedure.[58] The positive master for microfluidic device production was fabricated via standard photolithographic protocols: a SU-8 (Kayaku Advanced Materials, Inc.) layer was spin coated onto a silicon wafer and then exposed to UV light through a transparent photomask. A negative of such a master was replicated in polydimethylsiloxane (PDMS, Sylgard 184 Dow Corning). The final microfluidic device was molded from this PDMS replicate using the stiff, oil resistant photo-reactive resin NOA 83H (Norland optical adhesives). The devices were sealed with a microscopy glass slide and sandwiched with a coverslip to further increase the sample stability and avoid deformation of the channel at higher pressures. Such deformations are a typical problem among conventionally used PDMS devices.[15] The inlet of the microfluidic device was connected to a high-precision, pulsation-free syringe pump (neMESYS, Cetoni GmbH) that enabled fluid injection at a controlled volumetric flow rate. The outlet was connected to a liquid reservoir at the same height as the microfluidic device to avoid gravitational counter pressure. A board-mounted differential pressure sensor (26PC series, Honeywell) was installed between the inlet and outlet of the microfluidic device to measure the hydrodynamic pressure drop inside the microfluidic channel. Prior to the measurements, the pressure sensor was calibrated using a pressure-controlled pump (MFCS-EZ, Fluigent). The microfluidic device was placed on an inverted MeF3 microscope (Reichert-Jung) illuminated by a light-emitting diode (LED) light source in transmission and images were captured using a 16 Bit-sCMOS camera (PCO Panda 4.2) at a frame rate of 40 fps and a pixel resolution of (2048 × 2048) pixels. The microfluidic experiments were conducted at room temperature of (20 ± 1) °C. The microfluidic geometry was initially fully saturated with dodecane. Subsequently, dodecane was flushed out of the main channels by the respective invading phase at the lowest applied flow rate of 0.5 μ l/min but remained entrapped in the side channel. For each set of experiments, the flow rate of the invading phase was gradually increased in steps of 0.5 μl/min until it reached a critical flow rate where fluctuation of the fluid–fluid interface could be detected. The flow rate was increased further in steps of 1.0 μl/min until complete desaturation of the side channel. To ensure a fully developed steady-state flow while recording fluid-fluid interface fluctuations, we used the simultaneously measured pressure signal as a reference and started recording at each flow rate after the pressure reached a stable plateau.

C. Preparation and physical properties of working fluids

We used viscoelastic aqueous solutions that contained 1000 ppm (0.1 w%) or 2000 ppm (0.2 w%) of partially hydrolyzed polyacrylamide

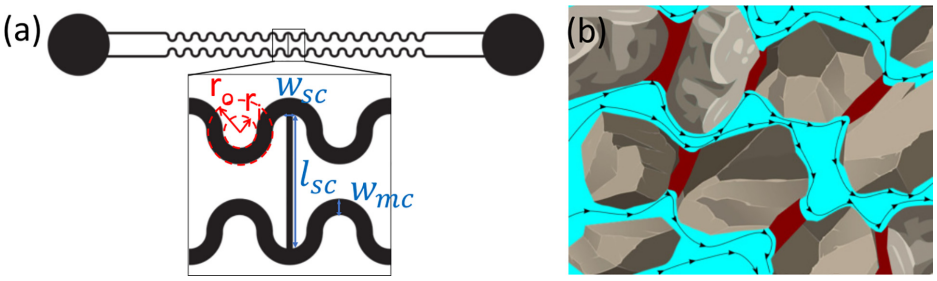

FIG. 1. Sketches of the microfluidic geometry (a) and a typical oil entrapment in a porous medium (b).

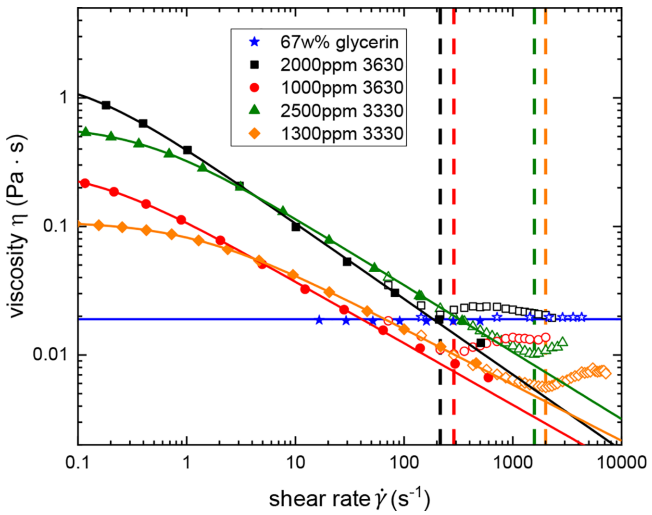

FIG. 2. The (shear) viscosity $\eta(\dot{\gamma})$ measured using a rheometer (filled symbols) and apparent viscosities calculated from *in situ* pressure measurements (open symbols). Lines are fits to the Carreau–Yasuda model. Dashed lines indicate the critical shear rates $\dot{\gamma}_{crit}$, where the viscosities calculated from *in situ* pressure measurements deviate from the bulk values.

(HPAM) Flopaam 3630 (SNF Floerger) and 1300 ppm (0.13 *w*%) or 2500 ppm (0.25 *w*%) Flopaam 3330 (SNF Floerger) as invading fluids in our microfluidic experiments. The molecular weights of the HPAM polymers Flopaam 3630 and 3330 are (18.7 ± 2.0) and (6.5 ± 2.0) MDa, respectively, according to the manufacturer. The concentrations of the respective polymer solutions were adjusted to provide similar shear viscosities despite their different degrees of elasticity (Figs. 2 and 3). Following a standard protocol,[59] we initially prepared a stock solution with 5000 ppm of the appropriate polymer in a "brine" solution composed of ultrapure water with 1000 ppm NaCl and 100 ppm $CaCl_2$. The stock solution was filtered to avoid the presence of any undissolved polymer or salt particles and subsequently diluted to the desired concentration by adding brine solution. To avoid degradation of the polymer solutions, the diluted solutions were renewed every three days and the respective stock solution every four weeks. By applying the Huggins–Kraemer method[60] using rotational shear rate ramp measurement results (data not shown), we determined the critical overlap concentrations to be $c^*_{3630} \approx 82$ ppm and $c^*_{3330} \approx 137$ ppm and the corresponding radii of gyration to be $Rg_{3630} \approx 441$ nm and $Rg_{3330} \approx 266$ nm for Flopaam 3630 and Flopaam 3330, respectively. Because the polymer concentrations used in our microfluidic experiments were at least ten times greater than c^*, we could safely presume to be in the semi-dilute regime. A characteristic exponent of 3/2 calculated by scaling the respective zero-shear viscosity as a function of the polymer concentration (data not shown) confirmed that we remained in the entangled regime for all utilized polymer solutions.[61] As a Newtonian reference case, an aqueous glycerin solution was prepared by adding 67 *w*% glycerin (Grüssing GmbH) to ultrapure water. The defending phase in all experiments was dodecane (Merck) with a constant dynamic viscosity $\eta_{dodecane} = 1.4$ mPa·s. First, dodecane was filtered three times in a column of aluminum oxide powder (Al_2O_3, Sigma Aldrich) to remove any potential surface-active contaminants. To increase the optical contrast of the fluids in the microfluidic setup, 0.5 *w*% of the non-surface-active dye oil-red-o (Sigma Aldrich) was added to the purified dodecane. For the visualization of path lines, 0.01 *w*% green fluorescent particles (2 μm, FluoroMax, Thermo Fisher) were added to the respective polymer solution and imaged via fluorescence microscopy. We confirmed that neither of these additives altered the physical or rheological properties of the utilized fluids. We measured densities of $\rho_P = (1.00 \pm 0.01)$ g/cm^3 and $\rho_G = (1.18 \pm 0.01)$ g/cm^3, respectively, for the aqueous polymer and glycerin solutions using a pycnometer. The respective interfacial tensions against dodecane were determined to be $\sigma_P = (50 \pm 1)$ mN/m and $\sigma_G = (32 \pm 1)$ mN/m via the pendant drop method using a contact angle measurement device (OCA 25, DataPhysics). The advancing and receding contact angles of the aqueous polymer and glycerin solutions on glass and the NOA 83H-surface in a surrounding dodecane phase were in all cases determined to be $\theta_{adv} = (125 \pm 4)^\circ$ and $\theta_{rec} = (59 \pm 6)^\circ$, respectively, via the sessile drop needle-in method using the contact angle measurement device (OCA 25, DataPhysics).

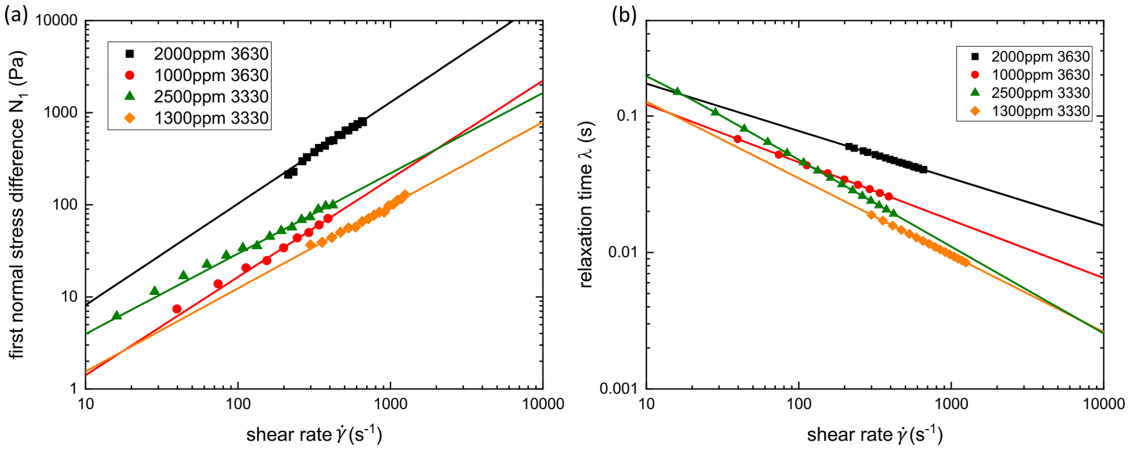

FIG. 3. The (a) first normal stress difference N_1 and (b) relaxation time λ as functions of the shear rate $\dot{\gamma}$. The lines in figures (a) and (b) are extrapolated power-law fits of N_1 and extrapolated Carreau fits of λ.

D. Viscoelastic fluid model

A representative fluid model was needed to describe the specific rheological properties of our viscoelastic polymer solutions in the semi-dilute regime and to provide quantitative interpretation of the experimental results. The general approach of describing viscoelastic fluids is to include viscoelastic properties via a total stress tensor $\mathbf{T} = \mathbf{T_1} + \mathbf{T_2}$, where the index "1" identifies a viscoelastic component and the index "2" a purely viscous component.[62] After defining a total viscosity $\eta = \eta_1 + \eta_2$ and a deformation rate tensor $\mathbf{D} = 1/2(\nabla \mathbf{u} + [\nabla \mathbf{u}]^{\mathrm{T}})$ derived from the velocity tensor **u,** we can estimate the solvent contribution to the total stress in a viscoelastic solution, i.e., the stress response that corresponds to the flow at vanishing degrees of elasticity, as $\mathbf{T_2} = 2\,\eta_2\,\mathbf{D}$. The viscoelastic contribution $\mathbf{T_1}$ is defined for each type of viscoelastic fluid model. In this work, we used the White–Metzner fluid constitutive model[63–65] as a representative framework for our polymer solutions. We chose this model because it is suitable for describing the non-quadratic first normal stress difference $N_1(\dot{\gamma})$ and the strong shear thinning viscosities of the HPAM solutions used in our experiments.[66–68] The White–Metzner fluid model computes $\mathbf{T_1}$ from

$$\mathbf{T_1} + \lambda \overset{\nabla}{\mathbf{T_1}} = 2\,\eta_1(\dot{\gamma})\,\mathbf{D}, \tag{1}$$

where λ and η_1 are the relaxation time and the viscosity of the polymer contribution, respectively; $\overset{\nabla}{\mathbf{T_1}}$ is the upper convected time derivative; and $\dot{\gamma}$ is the shear rate [defined as $\dot{\gamma} = \sqrt{2\,tr(\mathbf{D}^2)}$] that can be calculated from the velocity field and the rate of deformation tensor $\mathbf{D}$.[69]

To represent the shear-dependent total viscosities $\eta(\dot{\gamma})$ of the HPAM solutions, we applied the Carreau–Yasuda model, which is commonly utilized for this type of polymer,[67] i.e.,

$$\eta(\dot{\gamma}) - \eta_\infty = (\eta_0 - \eta_\infty)\left[1 + (\Lambda\dot{\gamma})^a\right]^{\frac{n-1}{a}}. \tag{2}$$

Here, η_0 and η_∞ are the zero-shear viscosity and viscosity at infinite shear rates, respectively; Λ is the characteristic time; n is the power-law exponent associated with the degree of shear thinning; and a is a transition control factor.

The shear-dependent relaxation time $\lambda(\dot{\gamma})$ is calculated from the shear viscosity, $\eta(\dot{\gamma})$, and the first normal stress difference, N_1, as follows:

$$\lambda(\dot{\gamma}) = N_1/2[\eta(\dot{\gamma}) - \eta_0]\dot{\gamma}^2. \tag{3}$$

The shear-dependent behavior of the relaxation time is described by the Careau model with λ_0 as the longest relaxation time as follows:

$$\lambda(\dot{\gamma}) = \frac{\lambda_0}{\left[1 + (\Lambda\dot{\gamma})^2\right]^{\frac{n-1}{2}}}. \tag{4}$$

III. RESULTS AND DISCUSSION

With our microfluidic experiments, we sought to understand the role of the elasticity of a viscoelastic polymer solution in the enhanced mobilization of capillary entrapments in porous media. To understand the effects of rheological properties on the flow and displacement processes, we first characterized our polymer solutions.

A. Rheological characterization

The polymer solutions selected in this work are known to exhibit strong shear rate dependence in the semi-dilute regime with regard to both the viscosity and relaxation time. To characterize their rheological properties, we conducted a set of rheological measurements to determine the shear-dependent viscosity $\eta(\dot{\gamma}))$ (Fig. 2) and first normal stress difference $N_1(\dot{\gamma})$ [Fig. 3(a)] using a Haake Mars 40 rheometer. Further details on the experimental measurement protocols can be found in the Appendix as well as the results of the frequency sweep tests.

The viscosity measurements in Fig. 2 are fitted to the Carreau model according to Eq. (2). The fitting parameters are summarized in Table I. The value of η_∞ was set to zero in all four fits. The shear-dependent relaxation time $\lambda(\dot{\gamma})$, plotted in Fig. 3(b), is calculated according to Eq. (3) using the viscosity data $\eta(\dot{\gamma})$ (Fig. 2) and the first normal stress difference N_1 [Fig. 3(a)]. The relaxation time $\lambda(\dot{\gamma})$ is fitted to the Carreau model [Eq. (4)]. The maximum relaxation times are $\lambda_0 \approx 1.2$ s (2000 ppm 3630), $\lambda_0 \approx 1.2$ s (1000 ppm 3630), $\lambda_0 \approx 0.4$ s (2500 ppm 3330), and $\lambda_0 \approx 0.5$ s (1300 ppm 3330).

B. Interfacial fluctuations and mobilization of capillary entrapment

The unique design of our microfluidic geometry [Fig. 1(a)] and high spatiotemporal optical resolution enabled us to focus on the interactions between the flow in the serpentine channel and the fluid–fluid interface of oil entrapped at the side channel, as depicted in Fig. 4(a) (Multimedia view). To this end, fluid–fluid interface time series were captured at various shear rates. The shear rate in serpentine channels is approximated by $\dot{\gamma} = 4Q/(\pi\, r^3)$ with the equivalent radius $r = \sqrt{(w_{mc}\, h)/\pi}$,[70] where w_{mc} and h are the width and height of the serpentine channels, respectively. The saturation S of the oil in the side channel and the fluctuating motion of the fluid–fluid interface could be acquired from the recorded time series. The saturation S was defined as the area of the oil column at the end of each step, normalized by the area of the oil column in the first step. Desaturation was initiated once the fluid–fluid interface was depinned from the edges of the side channel and $S < 1$. Interfacial motion was described quantitatively based on the motion of the center of mass, δY, of the entrapped

TABLE I. Fitting parameters of the Carreau–Yasuda model for viscosity: η_0 is the zero-shear viscosity; Λ is the characteristic time; a is a transition control factor; and n is the power-law exponent associated with the degree of shear thinning.

Polymer	η_0 (Pa·s)	Λ (s)	a	n
2000 ppm 3630	1.535 ± 0.011	9.45 ± 0.81	1.07 ± 0.05	0.41 ± 0.02
1000 ppm 3630	0.284 ± 0.004	6.89 ± 0.32	1.03 ± 0.06	0.52 ± 0.01
2500 ppm 3330	0.612 ± 0.003	2.43 ± 0.16	0.99 ± 0.06	0.48 ± 0.01
1300 ppm 3330	0.109 ± 0.001	0.81 ± 0.03	0.90 ± 0.02	0.56 ± 0.01

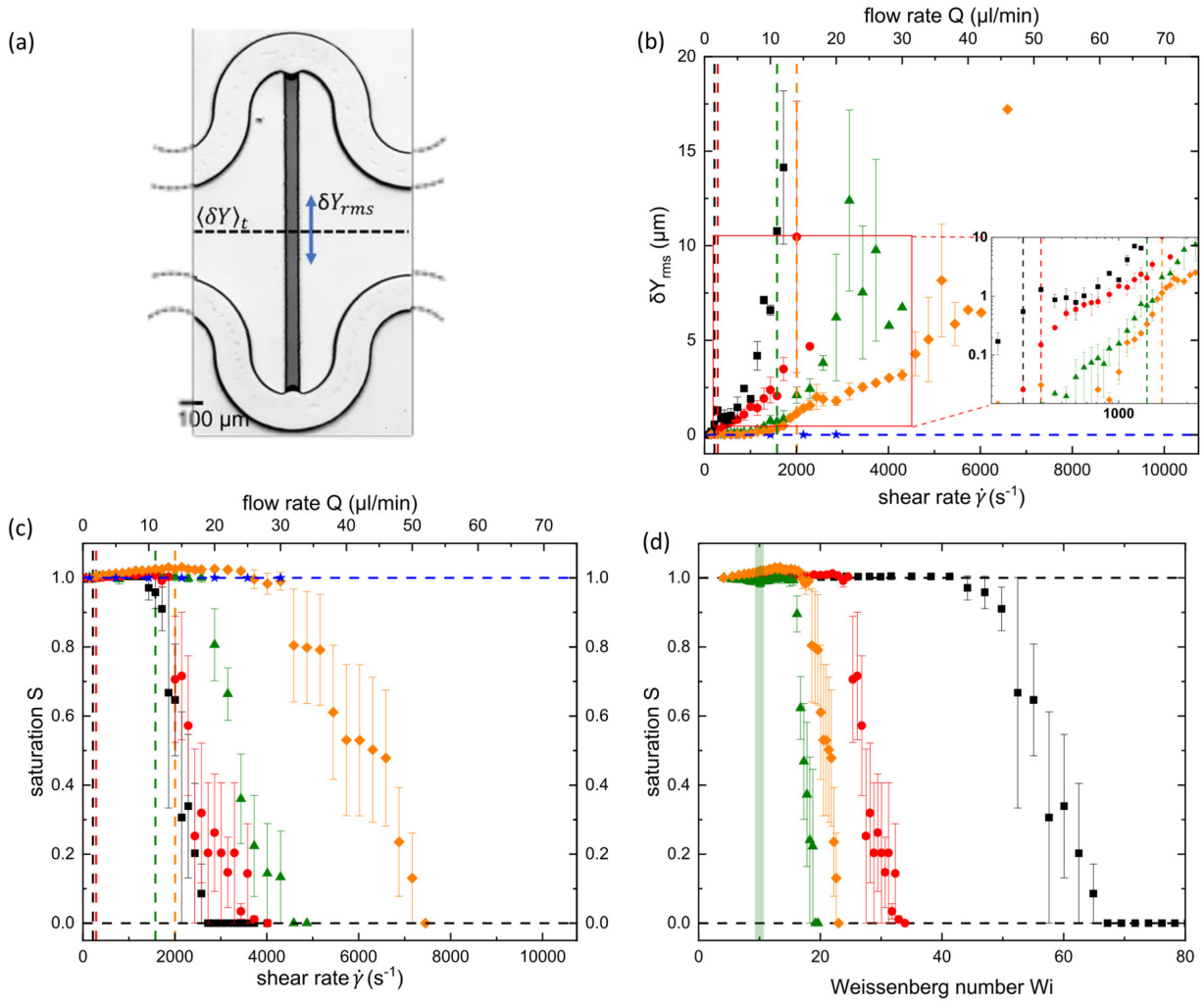

FIG. 4. (a) Optical image of microfluidic geometry. (b) Root-mean square (rms) of δY_{rms} The inset shows a magnified view of the initial values above $\delta Y_{rms} \approx 0.015\,\mu$m (marked by the red box). [(c) and (d)] Remaining oil saturation S in the side channel as a function of the applied flow at various (c) shear rates and (d) Weissenberg numbers. The vertical dashed lines in figures (b) and (c) as well as the green area in figure (d) indicate the onset of purely elastic instability. The symbols in figures (b)–(d) represent the experimental data for 67 w% glycerin (★), 2000 ppm Flopaam 3630 (■), 1000 ppm Flopaam 3630 (●), 2500 ppm Flopaam 3330 (▲), and 1300 ppm Flopaam 3330 (◆). Multimedia view: https://doi.org/10.1063/5.0071556.1

oil column. To quantify the strength of interfacial motion, we calculated the root mean square δY_{rms} for each shear rate and plotted the results in Fig. 4(b). As shown in the inset of Fig. 4(b), for $\delta Y_{rms} > 0.015\,\mu$m (i.e., for δY_{rms} values exceeding the noise level of the experimental setup), optically visible motion of the fluid–fluid interface that increases with the shear rate is clearly detectable. At the lowest applied shear rate of $\dot{\gamma} \approx 72\ s^{-1}$, the fluid–fluid interface is stationary for all utilized invading fluids. When glycerin solution is the invading phase, the fluid–fluid interface remains stationary across the full range of applied shear rates. Despite the rather high glycerin solution viscosity, no oil displacement is observed from the side channel [Fig. 4(c)]. However, when a viscoelastic polymer solution is the invading phase, the fluid–fluid interface begins to wobble above a certain shear rate. The intensity of this wobbling motion increases monotonically as the shear rate increases further. The higher the polymer molecular weight and concentration, i.e., the higher the degree of elasticity, the smaller the corresponding shear rate at which wobbling is initially detected. Eventually, the displacement of the entrapped oil phase from the side channel is initiated for all utilized polymer solutions when the fluid–fluid interface fluctuations are sufficiently intense [Fig. 4(c)]. As with the onset of interfacial fluctuations, the higher the elasticity of the polymer solution, the lower the critical shear rate at which displacement initiates. The large values of δY_{rms} and their respective error bars after the onset of displacement stem from the fact that two different types of motions contribute to δY_{rms} at this stage. These motions are the fluctuation of the fluid–fluid interface that is already visible at lower flow rates and the back-and-forth motion of the remaining oil column in the side channel that contributes at larger flow rates.

The dashed vertical lines in Figs. 4(b) and 4(c) correspond to the critical shear rates $\dot{\gamma}_{crit}$ that indicate the onset of increased flow resistance, as determined from the deviation of the apparent viscosity from the bulk shear viscosity in Fig. 2. Here, the apparent viscosity of each invading fluid is estimated from pressure drop measurements made between the inlet and outlet of the microfluidic device, $\bar{P}_{in-out}$, using the Hagen–Poiseuille equation for channels with rectangular cross sections. Because the maximum Reynolds number in our experiments is on the order of $Re \sim \mathcal{O}(10^0)$, potential inertial contributions to the observed increase in flow resistance can be neglected safely and it can be associated with so-called purely elastic instability at low Reynolds numbers.[14,50]

For the two Flopaam 3330 solutions, the wobbling motion starts at shear rates well below $\dot{\gamma}_{crit}$ [Fig. 4(b)]. This suggests that these initial fluctuations may have different physical origins than the purely elastic instability. The onset of elastic instability appears at similar critical Weissenberg numbers (the ratio of elastic and viscous forces) $Wi_{crit} = \lambda(\dot{\gamma}_{crit})\,\dot{\gamma}_{crit}$, as noted in Table II. This suggests that a certain ratio of elastic to viscous forces must be achieved in a given geometry to initiate purely elastic instability, independent of the molecular weight and polymer concentration. However, the desaturation curves plotted as functions of the Weissenberg number in Fig. 4(d) do not collapse, and no consistent Weissenberg number can be assigned to the onset of displacement. In particular, the respective onsets of displacement for the two polymer solutions that include Flopaam 3630 (high molecular weight) are shifted remarkably toward higher Weissenberg numbers than the two Flopaam 3330 solutions. These observations imply a more complex displacement mechanism with respect to the elasticity of the invading fluids.

Because there is no displacement in the case of a fully laminar flow of the glycerin solution, during the entire range of the experiments, it is evident that the magnitude of pressure, $\bar{P}_{in-out}$, cannot drive displacement. Indeed, the displacement mechanism can be explained with respect to the fluctuating component of pressure, $P'(t)$, in serpentine channels. These fluctuations occur because of the unstable nature of viscoelastic flow driven by the elasticity-induced instability at high shear rates. At any position in the channel, the instantaneous pressure, $P(t)$, can be treated as $P(t) = \langle P \rangle_t + P'(t)$, where $\langle P \rangle_t$ is the time-averaged steady-state mean value of the pressure at this position. Due to a common inlet and outlet and the symmetry of our microfluidic geometry, $\langle P \rangle_t$ cancels out, leaving the difference in fluctuating pressure components between both ends of the side channel to overcome the capillary pressure that traps the oil in place. Because there is no direct access to the local instantaneous pressure, $P(t)$, in our experimental setup, $P'(t)$ cannot be evaluated directly. Instead, we can hypothesize that the local pressure fluctuations correlate directly with the corresponding time averaged steady-state mean pressure, i.e., $P'(t) \propto \langle P \rangle_t$. Assuming a constant pressure gradient along the microfluidic geometry, $\langle P \rangle_t$ can be assessed directly from the experimentally measured pressure difference $\bar{P}_{in-out}$. Furthermore, the fluctuating component, $P'(t)$, is reflected directly by the intensity of the observed interfacial fluctuations. Our hypothesis is supported by the fact that the intensity of interfacial fluctuations increases in proportion with the average pressure difference between the inlet and outlet, $\bar{P}_{in-out}$, of the microfluidic geometry [Fig. 5(a)]. Hence, we can consider $\bar{P}_{in-out}$ as a measure of $\langle P \rangle_t$ and the δY_{rms} values as a measure of pressure fluctuation intensities at both ends of the side channel. The plot of saturation as a function of $\bar{P}_{in-out}$ shown in Fig. 5(b) shows that the remaining saturations of all invading polymer solutions collapse into a single curve and displacement of the entrapment occurs within a narrow pressure range (indicated by the red area in Fig. 5). A comparison of the data shown in Figs. 4(b) and 4(c) indicates that the displacement starts at a fluctuation intensity larger than $\delta Y_{rms} \approx 3\,\mu$m, as shown via the dashed lines in Fig. 5(a) and in the inset of Fig. 5(b), respectively. In fact, as indicated in the inset of Fig. 5(b), when saturation is plotted as a function of δY_{rms}, the displacement starts at similar fluctuation intensities $\delta Y_{rms} \approx 3\,\mu$m, i.e., in a similar range of pressure fluctuations, regardless of the polymer concentration and molecular weight. It can therefore be concluded that due to the unstable nature of the flow, the pressure fluctuations provide the pressure required to overcome the capillary threshold of the entrapment once they are strong enough.

TABLE II. Overview of the experimentally preset flow rate Q_{crit}, the approximate shear rate $\dot{\gamma}_{crit}$, and the Weissenberg number Wi_{crit} at the onset of purely elastic instability. The specified error margins are determined based on the nominal precision of the microfluidic pump and rheometer, as well as dimensional uncertainty within the microfluidic device.

Polymer	Q_{crit} (μl/min)	$\dot{\gamma}_{crit}$ (s^{-1})	Wi_{crit}
2000 ppm 3630	1.5 ± 0.2	215 ± 30	12.8 ± 2.9
1000 ppm 3630	2.0 ± 0.2	287 ± 21	11.2 ± 1.8
2500 ppm 3330	11.0 ± 0.2	1576 ± 139	13.0 ± 0.1
1300 ppm 3330	14.0 ± 0.2	2006 ± 192	13.0 ± 0.1

C. Elasticity-induced phenomena in serpentine channels

To illustrate the underlying elasticity-induced flow features that cause the observed unstable flow and motion of the fluid–fluid interface, we visualized flow path lines by adding fluorescent particles to the invading polymer phase. Figure 6 (Multimedia view) shows the viscoelastic flow path lines for 2500 ppm Flopaam 3330, as visualized using fluorescence imaging. At $\dot{\gamma} \approx 143\,s^{-1} < \dot{\gamma}_{crit}$ in Fig. 6(a), we observe a laminar flow, in which the flow path lines follow the curvature of the channel. At increased $\dot{\gamma}$ but below $\dot{\gamma}_{crit} \approx 1576\ s^{-1}$, in Figs. 6(b) and 6(c), the path lines become slightly asymmetric with reference to a central vertical line. At this stage, visible but mild fluid–fluid interface fluctuations occur [Fig. 6(c)]. After the onset of purely elastic instability, $\dot{\gamma} > \dot{\gamma}_{crit}$, the base flow exhibits characteristics of turbulent flow such as chaotic motion of fluorescent particles and semi-3D effects in the form of crossing path lines [Figs. 6(d)–6(f)]. With further increase in $\dot{\gamma}$, the intensity of the turbulent flow is amplified and accompanied by eventual displacement of oil from the side channel [Figs. 6(e) and 6(f)]. As indicated in Fig. 6(f), no steady path line is established in the perpendicular side channel and only random particle motion is observed temporarily. The latter observation confirms the presence of an instantaneous pressure difference between the two ends of the side channel.

Figure 7(a) illustrates an example PSD analysis of δY extracted from the optical images of 2500 ppm Flopaam 3330. We observe a rather flat plateau at the lowest shear rate $\dot{\gamma} \approx 72\,s^{-1}$ s, where the fluid–fluid interface remains stationary. At $\dot{\gamma} \approx 716\,s^{-1}$, i.e., below $\dot{\gamma}_{crit}$, the PSD curve continues to be a rather flat plateau even though interfacial fluctuations are detected optically at this shear rate

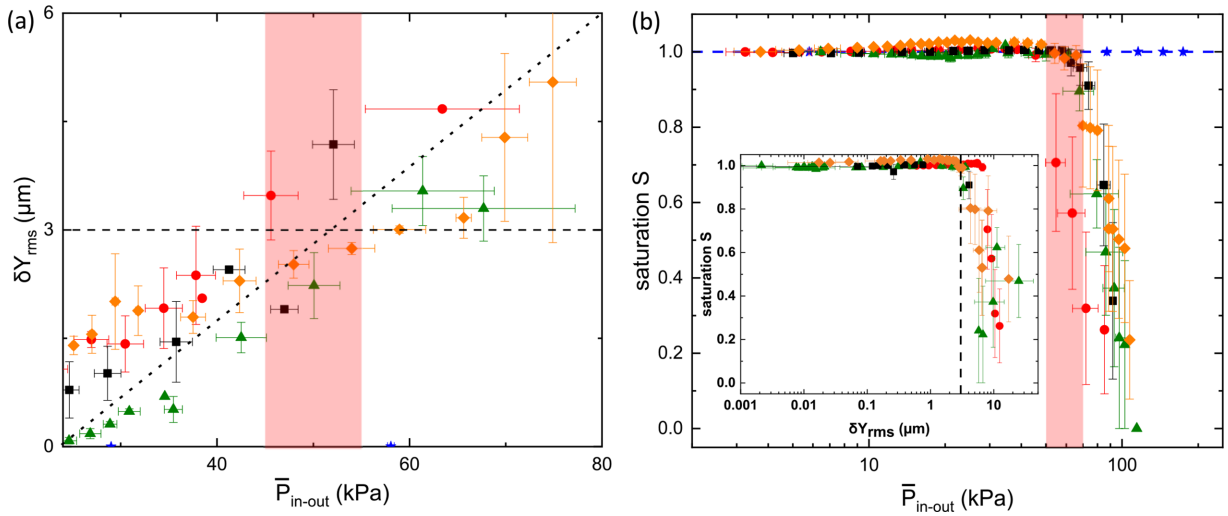

FIG. 5. (a) The fluctuation intensity δY_{rms} and (b) remaining oil saturation S as functions of the measured pressure difference $\bar{P}_{in-out}$. The inset in figure (b) shows the saturation S as function of δY_{rms}. The horizontal dashed lines in figure (a) and the inset in figure (b) indicate $\delta Y_{rms} \approx 3\ \mu$m, where we observe the onset of displacement in Fig.4(b). The red areas in figures (a) and (b) refer to the pressure ranges associated with the onset of displacement. The symbols in figures (a) and (b) represent the experimental data for 67 w% glycerin (★), 2000 ppm Flopaam 3630 (■), 1000 ppm Flopaam 3630 (●), 2500 ppm Flopaam 3330 (▲), and 1300 ppm Flopaam 3330 (◆).

[Fig. 4(b)]. This suggests an additional phenomenon induced by polymer solution elasticity prior to the onset of purely elastic instability. At further increased shear rates, close to $\dot{\gamma}_{crit} \approx 1576\ s^{-1}$ and above, power-law decay is observed with an exponent $\beta > 3$. In general, at shear rates above the respective critical values for the various polymer types and concentrations, power-law decay with an exponent within $3.3 \leq \beta \leq 3.8$ is detected in Figs. 7(b)–7(d). This is also in agreement with the exponent $\beta \approx 3.4$ reported by Mitchell *et al.*,[54] who performed a similar analysis. Based on this, we can conclude that above the respective values of $\dot{\gamma}_{crit}$, as identified in Fig. 2, the characteristic features of purely elastic instability are indeed reflected in the observed fluctuating motion of the fluid–fluid interface.

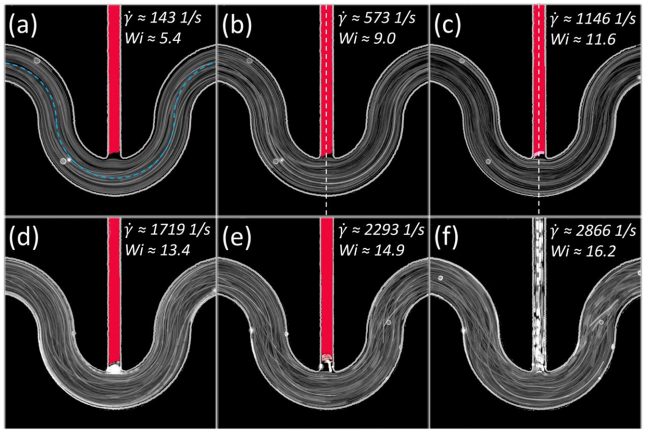

FIG. 6. [(a)–(f)] Stacks of 32 consecutive path line images of flow in the serpentine channel. The fluid is 2500 ppm Flopaam 3330 and the images are obtained via fluorescence microscopy. The flow direction is from left to right. The dashed blue line in figure (a) is a guide for the eye and marks the radius of curvature of the serpentine channel. The white vertical dashed lines in figures (b) and (c) are references for symmetry. The entrapped oil phase is colored red artificially for easier identification. The pink area in figures (c)–(e) indicates the moving fluid–fluid interface. Multimedia view: https://doi.org/10.1063/5.0071556.2

The observed interfacial fluctuations, out of plane particle motion, and slight flow path line asymmetry in Fig. 6(c) prior to the onset of purely elastic instability (more visible for Flopaam 3330) may be associated with elastic secondary flows, i.e., flows in the cross-stream direction that are much weaker than the flow in the main flow direction.[16,71,72] These types of secondary flows result from a difference between the curvatures of inner and outer bends of the serpentine channel, where the gradient of the first normal stress difference N_1 arises [Fig. 8(a)]. Consequently, the so-called "Hoop stress" emerges and drives the viscoelastic fluid toward inner bends at the top and bottom of the serpentine channel, where N_1 is the largest. The fluid is then pushed back to the outer part of the serpentine channel at the center plane to complete the formation of counter-rotating vortices in the out-of-plane cross section of the channel, as indicated by the dashed contours of potential secondary flow vortices in Fig. 8(a). Values of N_1 as a function of the normalized lateral distance along the dashed central line in Fig. 8(a) are shown in Fig. 8(b). As indicated in this figure, the N_1 difference between the inner and outer bends is continuously increased by increasing the shear rate, respectively, the Weissenberg number. However, due to the difficulty of solving the flow equation including the White–Metzger fluid model after the onset of purely elastic instability, the computational fluid dynamics (CFD) simulations are limited to low Weissenberg numbers. The out-of-plane moving particles, and thus the path lines deformed in the direction of flow toward the inner bend in the consecutive stacks of images observed experimentally in Figs. 6(b) and 6(c), are consistent with the direction of counter-rotating secondary flow vortices in the upper half of the channel [Fig. 8(a)] with the assumption that the focal plane of the objective is set slightly above the midplane with respect to the z-direction. Therefore, we can conclude that the visible but mild fluctuations of the fluid–fluid interfaces in Fig. 4(b) and the deviations from the laminar path lines in Fig. 6(c) occur because of the secondary flows. Such elastic secondary flows are present for all

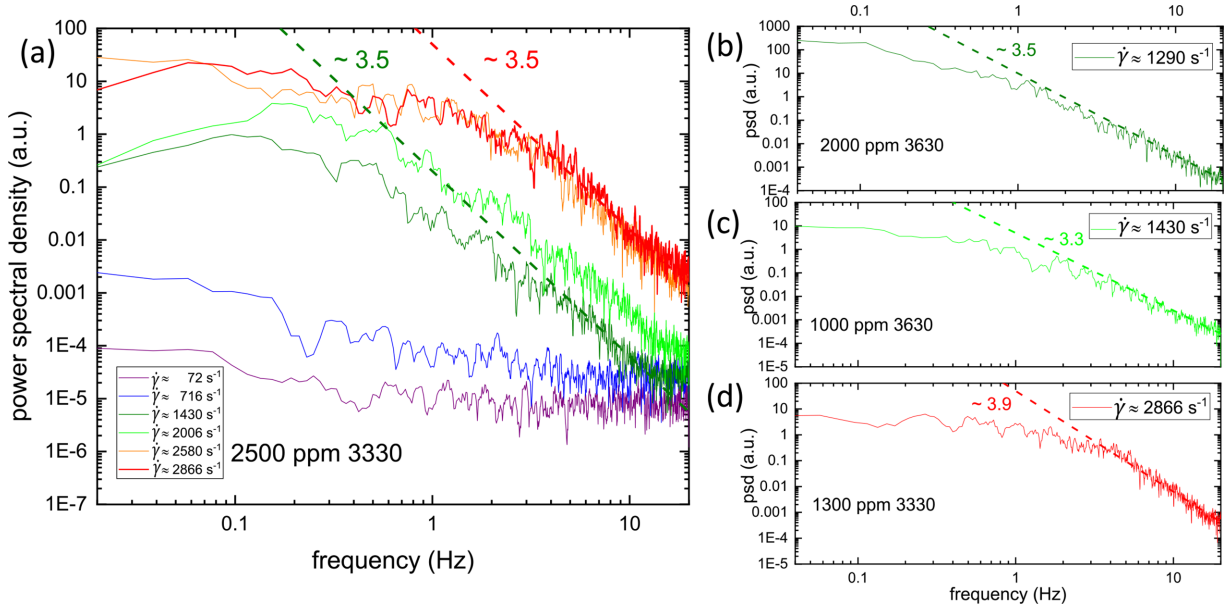

FIG. 7. PSD analysis of vertical fluctuation of the center position δY of (a) 2500 ppm Flopaam 3330 for various shear rates above and below the critical shear rate; (b) 2000 ppm Flopaam 3630; (c) 1000 ppm Flopaam 3630; and (d) 1300 ppm Flopaam 3330. The shear rates in figures (b)–(d) are selected to ensure that the flow is safely above the onset of purely elastic instability $\dot{\gamma}_{crit}$.

applied shear rates in the case of viscoelastic flow and their strength intensifies as the Weissenberg number increases.[17]

To study the evolution of flow toward a fully developed elastic turbulent state, the experimentally measured pressure drops were normalized using the corresponding values of a laminar reference flow and plotted as functions of the shear rate $\dot{\gamma}$ in Figs. 9(a) and 9(b) and as a function of the Weissenberg number Wi in Fig. 9(c). The pressure drops of the corresponding laminar reference flows were calculated using CFD simulations of imaginary fluids with the same shear thinning properties as the polymer solutions defined by the Carreau–Yasuda model, i.e., with no elastic component attributed to the total stress tensor. The normalized pressure is close to unity at lower shear rates, respectively, at $Wi < Wi_{crit}$. This verifies the laminar-flow regime at this stage. A steep monotonic increase is observed for all solutions above the onset of purely elastic instability. After this onset, the normalized pressure follows a convex shape in the case of Flopaam 3630 and a concave shape in the case of Flopaam 3330. The curve flattens slowly at the highest applied shear rates for all

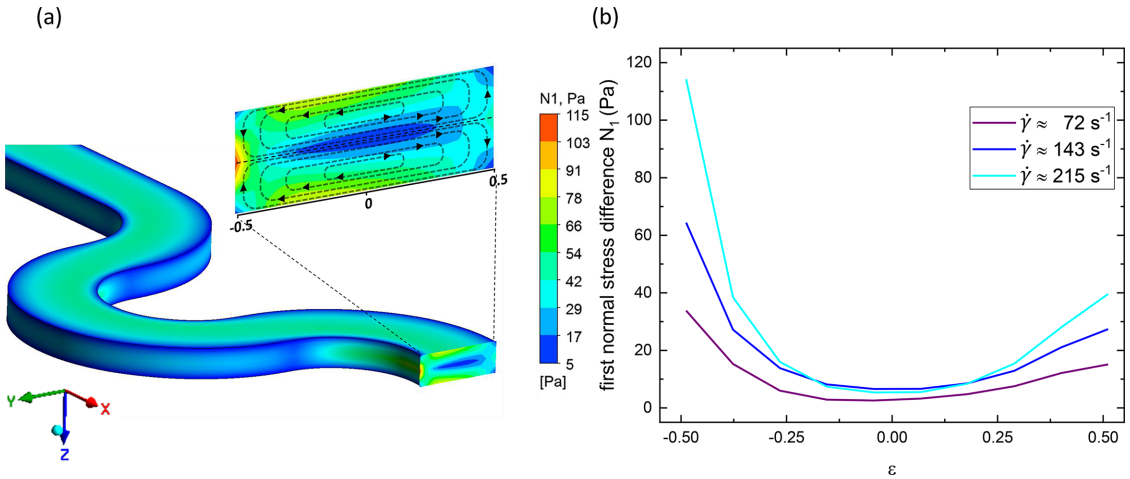

FIG. 8. (a) Sample distribution of the first normal stress difference N_1 within a vertical cross section of the serpentine channel obtained via CFD simulations using the White–Metzner model for 2500 ppm Flopaam 3330 at $\dot{\gamma} \approx 143\,s^{-1}$ and corresponding $Wi \approx 5.4$. The contours of potential secondary flow vortices are indicated by dashed lines, which are intended as guides to the eye. (b) N_1 at the central line of the cross section for increasing shear rates $\dot{\gamma} \approx 72\,s^{-1}$ s ($Wi \approx 4.2$), $\dot{\gamma} \approx 143\,s^{-1}$ ($Wi \approx 5.4$), and $\dot{\gamma} \approx 215\,s^{-1}$ ($Wi \approx 6.3$).

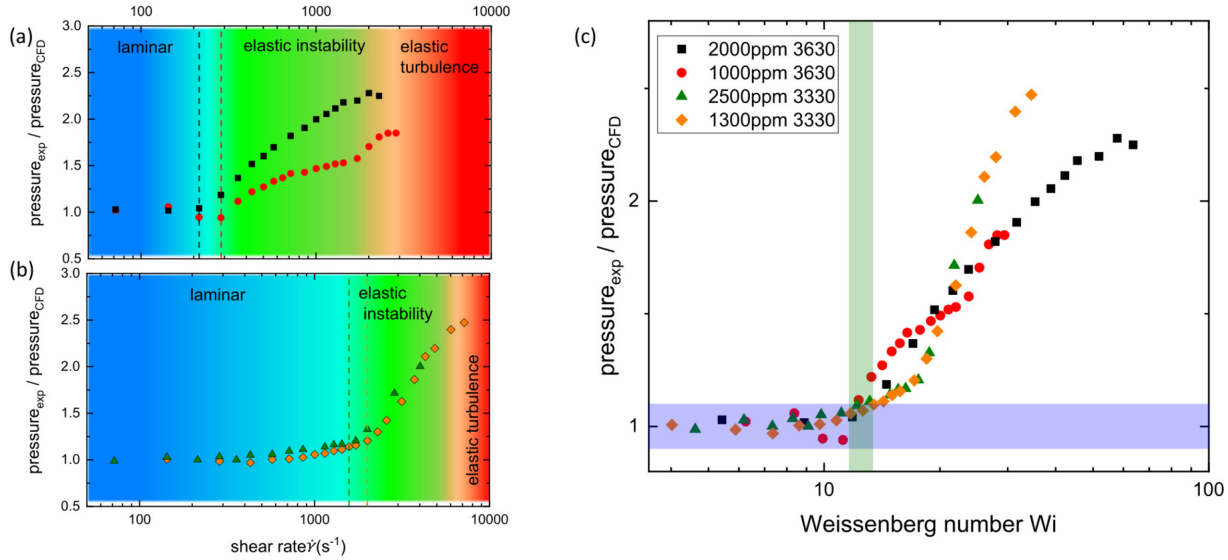

FIG. 9. The ratio of experimentally measured pressures to the computed steady-state pressure drops of imaginary fluids with the same shear thinning properties, as defined by the Carreau–Yasuda model. Evolution of flow from a laminar to a fully developed turbulent regime for the polymers (a) Flopaam 3630 and (b) Flopaam 3330 as function of the shear rate, and Weissenberg number (c). The symbols in figure (a) represent data for 2000 ppm Flopaam 3630 (■), and 1000 ppm Flopaam 3630 (●), while the symbols in (b) represent 2500 ppm Flopaam 3330 (▲), and 1300 ppm Flopaam 3330 (◆). The horizontal rectangle indicates the laminar regime, the vertical rectangle marks the onset of purely elastic instabilities.

the polymer solutions [Figs. 9(a) and 9(b)]. The latter behavior is interpreted in the literature as an indication of transition toward a fully developed turbulent regime.[7,16,73] The different curvatures of the evolving normalized pressures after the onset of purely elastic instability can be explained with respect to the relaxation time, i.e., degree of elasticity of polymer coils in the solutions. Larger polymer coils, i.e., Flopaam 3630, are more elastic and therefore stretch more easily during flow. This leads to an immediate and steep increase in normalized pressure, after the onset of purely elastic instability. Higher elasticity of polymers in the solution also leads to a fully developed turbulent state already at lower shear rates [Figs. 9(a) and 9(b)]. In the case of Flopaam 3630, the transition from laminar to fully developed turbulence occurs in the range of $\dot{\gamma} \approx 200$ s^{-1} to $\dot{\gamma} \approx 2000$ s^{-1}, whereas transition for Flopaam 3330 occurs between $\dot{\gamma} \approx 2000$ s^{-1} and $\dot{\gamma} \approx 6000$ s^{-1}. Comparing these shear rates to the shear rate range where we detect displacement of the capillary entrapment in our geometry, in Fig. 4(d), we note that the displacement coincides with transition toward the fully developed turbulent regime.

IV. CONCLUSION AND OUTLOOK

A single-entrapment microfluidic geometry was designed based on serpentine channels to mimic the essential features of flow in porous media, i.e., shear-dominated tortuous pathways. The unique microfluidic geometry and high optical and temporal resolution of our experiments allowed us to focus on the displacement of capillary entrapments (exclusively) by elastic stresses. We confirmed that the presence of purely elastic instabilities is reflected by the statistics of the interfacial fluctuations. Based on the power spectral density analysis, a characteristic exponent $\beta \approx 3.5$ was detected for shear rates that exceeded the onset of elastic instability. This led us to conclude that the mild interfacial fluctuations observed prior to the onset of purely elastic instability have a different origin and could be attributed to secondary flows induced by the gradient of the first normal stress difference due to the curvature of the serpentine channel. It was evident that a certain fluctuation intensity is required to overcome the capillary pressure threshold and initiate desaturation. The results of our experiments confirmed that displacement of the capillary entrapment is governed primarily by the randomness of base flow that arises from elastic instability. The results of our research show that, in our specific design, the displacement coincides with transition toward a fully developed turbulent regime regardless of the polymer molecular weight and concentration.

Displacement processes in actual porous media are more complex. Flow asymmetry in randomized porous media and heterogeneous pore-throat distributions lead to a wide range of capillary entrapment sizes as well as broad distributions of *in situ* flow velocities. This produces non-uniform viscous pressure fields. Therefore, a synergic effect of different elasticity-induced phenomena coupled with viscous forces can be expected to contribute to the mobilization of capillary entrapments. Thus, decoupling of these components requires further in-depth investigation into more complex model systems.

ACKNOWLEDGMENTS

We acknowledge the generous support of BP plc's ExploRe program. We would like to thank SNF Floerger, France for providing us the Flopaam polymers as well as Michael Batzel for assisting us with rheology measurements. We would like to take this opportunity to thank Professor Dr. Stephan Herminghaus and Dr. Martin Brinkmann for their stimulating discussions.

AUTHOR DECLARATIONS

Conflict of Interest

The authors have no conflicts of interest to disclose.

DATA AVAILABILITY

The data that support the findings of this study are available from the corresponding author upon reasonable request.

APPENDIX: RHEOLOGY PROTOCOLS

1. Rotational test

Shear viscosity of all polymer solutions and dynamic viscosity of the glycerin solution as shown in Fig. 2 of the main text were determined through a steady shear step test applying a standard protocol in stress-controlled mode using HAAKE MARS 40 rheometer and 60 mm cone plate geometry with 1° angle. To avoid air bubbles when placing the respective fluids between the cone and plate, we placed a small droplet at the tip of the cone to create a wetting film when bringing the cone and plate in contact. The temperature was set to $(20 \pm 0.2)^{\circ}$ C for all measurements to match the lab temperature.

2. First normal stress difference

The measurements of the first normal stress difference N_1 are shown in Fig. 10(a). At each step, first the normal force value is set to zero. To account for the drift caused by relaxation of the solution as well as the force measuring sensor in the device, the measuring geometry stays for 300 s at rest, followed by a constant rotation at fixed applied stress for 300 s. The respective polymer solution in the measuring geometry was surrounded by mineral oil to avoid inertial instabilities at the edges at higher rotation rates. The normal force values measured by the rheometer were corrected for inertia, $N_{inertia} = -0.075\pi\rho\Omega^2R^4$, and drift and converted to the first normal stress difference using $N_{1corr} = \frac{2F_n}{\pi R^2}$ in which F_n is the normal force measured by the rheometer; Ω, ρ, and R are the angular rotation, density, and the radius of the measuring geometry, respectively. An exemplary plot (four times repetitions) of first normal stress difference as a function of shear rate for 2000 ppm Flopaam 3630 is shown in Fig. 10(b).

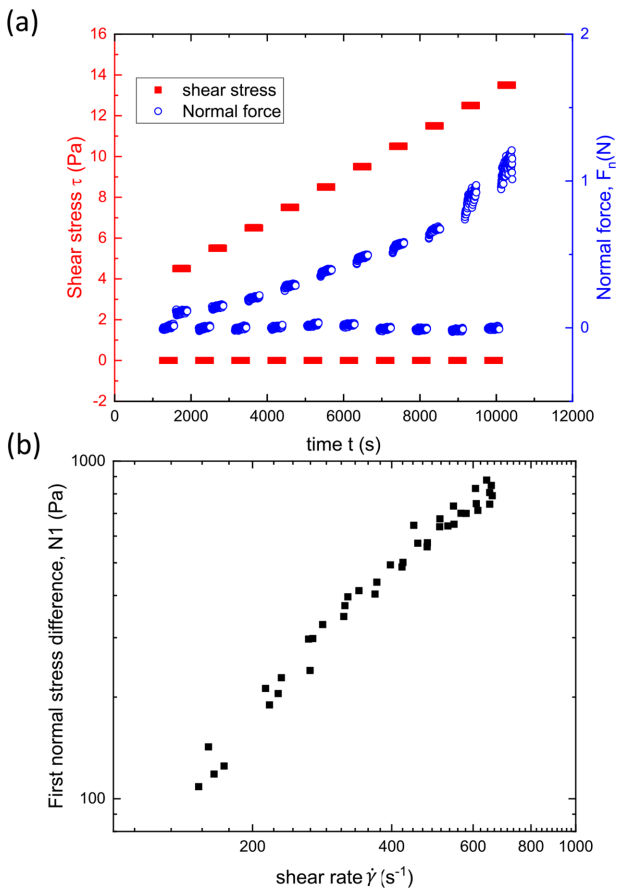

FIG. 10. Exemplary normal force measurement for 2000 ppm Flopaam 3630 (a) and corresponding first normal stress differences N_1 (b).

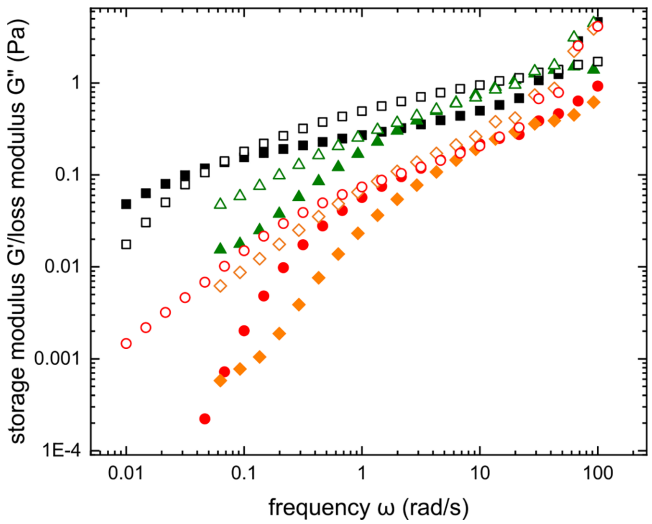

FIG. 11. Frequency sweep test for the utilized polymer solutions: 2000 ppm Flopaam 3630 (■), 1000 ppm Flopaam 3630 (●), 2500 ppm Flopaam 3330 (▲), and 1300 ppm Flopaam 3330 (◆). Filled symbols represent the storage modulus G' and open symbols represent the loss modulus G''.

3. Frequency sweep test

The small amplitude frequency sweep tests were performed using a standard protocol in stress-controlled mode. The stress amplitude was acquired priorly from a deformation amplitude sweep test to be safely in the linear viscoelastic range. To ensure minimum measurement error, the duration of measurements at each point was automatically adjusted based on the frequency. The results are shown in Fig. 11.

REFERENCES

[1]A. Groisman and V. Steinberg, "Mechanism of elastic instability in Couette flow of polymer solutions: Experiment," Phys. Fluids **10**, 2451–2463 (1998).
[2]V. Steinberg, "Elastic turbulence: An experimental view on inertialess random flow," Annu. Rev. Fluid Mech. **53**, 27–58 (2021).
[3]T. Burghelea, E. Segre, and V. Steinberg, "Elastic turbulence in von Karman swirling flow between two disks," Phys. Fluids **19**, 053104 (2007).
[4]Y. Jun and V. Steinberg, "Elastic turbulence in a curvilinear channel flow," Phys. Rev. E **84**, 056325 (2011).

[5]T. Burghelea, E. Segre, and V. Steinberg, "Validity of the Taylor hypothesis in a random spatially smooth flow," Phys. Fluids **17**, 103101 (2005).
[6]J. Davoudi and J. Schumacher, "Stretching of polymers around the Kolmogorov scale in a turbulent shear flow," Phys. Fluids **18**, 025103 (2006).
[7]A. Groisman and V. Steinberg, "Elastic turbulence in curvilinear flows of polymer solutions," New J. Phys. **6**, 29 (2004).
[8]Y. Jun and V. Steinberg, "Polymer concentration and properties of elastic turbulence in a von Karman swirling flow," Phys. Rev. Fluids **2**, 103301 (2017).
[9]A. Fouxon and V. Lebedev, "Spectra of turbulence in dilute polymer solutions," Phys. Fluids **15**, 2060–2072 (2003).
[10]A. Groisman and V. Steinberg, "Stretching of polymers in a random three-dimensional flow," Phys. Rev. Lett. **86**, 934–937 (2001).
[11]Y. Jun and V. Steinberg, "Power and pressure fluctuations in elastic turbulence over a wide range of polymer concentrations," Phys. Rev. Lett. **102**, 124503 (2009).
[12]V. Steinberg, "Scaling relations in elastic turbulence," Phys. Rev. Lett. **123**, 234501 (2019).
[13]T. Watanabe and T. Gotoh, "Power-law spectra formed by stretching polymers in decaying isotropic turbulence," Phys. Fluids **26**, 035110 (2014).
[14]A. Groisman and V. Steinberg, "Elastic turbulence in a polymer solution flow," Nature **405**, 53–55 (2000).
[15]X. Shi and G. F. Christopher, "Growth of viscoelastic instabilities around linear cylinder arrays," Phys. Fluids **28**, 124102 (2016).
[16]G. Yao, J. Zhao, H. Yang, M. A. Haruna, and D. Wen, "Effects of salinity on the onset of elastic turbulence in swirling flow and curvilinear microchannels," Phys. Fluids **31**, 123106 (2019).
[17]J. Zilz, R. J. Poole, M. A. Alves, D. Bartolo, B. Levaché, and A. Lindner, "Geometric scaling of a purely elastic flow instability in serpentine channels," J. Fluid Mech. **712**, 203–218 (2012).
[18]B. Traore, C. Castelain, and T. Burghelea, "Efficient heat transfer in a regime of elastic turbulence," J. Non-Newtonian Fluid Mech. **223**, 62–76 (2015).
[19]R. Whalley, W. Abed, D. Dennis, and R. Poole, "Enhancing heat transfer at the micro-scale using elastic turbulence," Theor. Appl. Mech. Lett. **5**, 103–106 (2015).
[20]W. M. Abed, R. D. Whalley, D. J. Dennis, and R. J. Poole, "Experimental investigation of the impact of elastic turbulence on heat transfer in a serpentine channel," J. Non-Newtonian Fluid Mech. **231**, 68–78 (2016).
[21]D.-Y. Li, X.-B. Li, H.-N. Zhang, F.-C. Li, S. Qian, and S. W. Joo, "Efficient heat transfer enhancement by elastic turbulence with polymer solution in a curved microchannel," Microfluid. Nanofluid. **21**, 10 (2017).
[22]H. Yang, G. Yao, and D. Wen, "Experimental investigation on convective heat transfer of shear-thinning fluids by elastic turbulence in a serpentine channel," Exp. Therm. Fluid Sci. **112**, 109997 (2020).
[23]T. Burghelea, E. Segre, I. Bar-Joseph, A. Groisman, and V. Steinberg, "Chaotic flow and efficient mixing in a microchannel with a polymer solution," Phys. Rev. E **69**, 066305 (2004).
[24]A. Groisman and V. Steinberg, "Efficient mixing at low Reynolds numbers using polymer additives," Nature **410**, 905–908 (2001).
[25]J. A. Pathak, D. Ross, and K. B. Migler, "Elastic flow instability, curved streamlines, and mixing in microfluidic flows," Phys. Fluids **16**, 4028–4034 (2004).
[26]H. Yang, G. Yao, and D. Wen, "Efficient mixing enhancement by orthogonal injection of shear-thinning fluids in a micro serpentine channel at low Reynolds numbers," Chem. Eng. Sci. **235**, 116368 (2021).
[27]A. Clarke, A. M. Howe, J. Mitchell, J. Staniland, and L. A. Hawkes, "How viscoelastic-polymer flooding enhances displacement efficiency," SPE J. **21**, 0675–0687 (2016).
[28]A. Rock, R. E. Hincapie, J. Wegner, and L. Ganzer, "Advanced flow behavior characterization of enhanced oil recovery polymers using glass-silicon-glass micromodels that resemble porous media," in *SPE Europec Featured at EAGE Conference and Exhibition* (OnePetro, 2017).
[29]R. E. Hincapie, A. Rock, J. Wegner, and L. Ganzer, "Oil mobilization by viscoelastic flow instabilities effects during polymer EOR: A pore-scale visualization approach," in *SPE Latin America and Caribbean Petroleum Engineering Conference* (OnePetro, 2017).
[30]C. A. Browne, A. Shih, and S. S. Datta, "Pore-scale flow characterization of polymer solutions in microfluidic porous media," Small **16**, 1903944 (2020).
[31]S. De, J. A. Kuipers, E. A. Peters, and J. T. Padding, "Viscoelastic flow past mono- and bidisperse random arrays of cylinders: Flow resistance, topology and normal stress distribution," Soft Matter **13**, 9138–9146 (2017).
[32]E. Hemingway, A. Clarke, J. Pearson, and S. Fielding, "Thickening of viscoelastic flow in a model porous medium," J. Non-Newtonian Fluid Mech. **251**, 56–68 (2018).
[33]B. Khomami and L. D. Moreno, "Stability of viscoelastic flow around periodic arrays of cylinders," Rheol. Acta **36**, 367–383 (1997).
[34]B. Qin, P. F. Salipante, S. D. Hudson, and P. E. Arratia, "Flow resistance and structures in viscoelastic channel flows at low re," Phys. Rev. Lett. **123**, 194501 (2019).
[35]B. Qin and P. E. Arratia, "Characterizing elastic turbulence in channel flows at low Reynolds number," Phys. Rev. Fluids **2**, 083302 (2017).
[36]M. Kumar and A. M. Ardekani, "Elastic instabilities between two cylinders confined in a channel," Phys. Fluids **33**, 074107 (2021).
[37]S. De, J. van der Schaaf, N. G. Deen, J. A. M. Kuipers, E. A. J. F. Peters, and J. T. Padding, "Lane change in flows through pillared microchannels," Phys. Fluids **29**, 113102 (2017).
[38]S. Varchanis, C. C. Hopkins, A. Q. Shen, J. Tsamopoulos, and S. J. Haward, "Asymmetric flows of complex fluids past confined cylinders: A comprehensive numerical study with experimental validation," Phys. Fluids **32**, 053103 (2020).
[39]D. M. Walkama, N. Waisbord, and J. S. Guasto, "Disorder suppresses chaos in viscoelastic flows," Phys. Rev. Lett. **124**, 164501 (2020).
[40]C. C. Hopkins, S. J. Haward, and A. Q. Shen, "Tristability in viscoelastic flow past side-by-side microcylinders," Phys. Rev. Lett. **126**, 054501 (2021).
[41]S. De, J. A. Kuipers, E. A. Peters, and J. T. Padding, "Viscoelastic flow simulations in model porous media," Phys. Rev. Fluids **2**, 1–21 (2017).
[42]J. J. J. Gillissen, "Viscoelastic flow simulations through an array of cylinders," Phys. Rev. E **87**, 023003 (2013).
[43]E. M. Ekanem, S. Berg, S. De, A. Fadili, T. Bultreys, M. Rücker, J. Southwick, J. Crawshaw, and P. F. Luckham, "Signature of elastic turbulence of viscoelastic fluid flow in a single pore throat," Phys. Rev. E **101**, 042605 (2020).
[44]F. J. Galindo-Rosales, L. Campo-Deaño, F. T. Pinho, E. Van Bokhorst, P. J. Hamersma, M. S. Oliveira, and M. A. Alves, "Microfluidic systems for the analysis of viscoelastic fluid flow phenomena in porous media," Microfluid. Nanofluid. **12**, 485–498 (2012).
[45]M. Kumar, S. Aramideh, C. A. Browne, S. S. Datta, and A. M. Ardekani, "Numerical investigation of multistability in the unstable flow of a polymer solution through porous media," Phys. Rev. Fluids **6**, 033304 (2021).
[46]P. Pakdel and G. H. McKinley, "Elastic instability and curved streamlines," Phys. Rev. Lett. **77**, 2459–2462 (1996).
[47]G. H. McKinley, P. Pakdel, and A. Öztekin, "Rheological and geometric scaling of purely elastic flow instabilities," J. Non-Newtonian Fluid Mech. **67**, 19–47 (1996).
[48]S. S. Datta, A. M. Ardekani, P. E. Arratia, A. N. Beris, I. Bischofberger, J. G. Eggers, J. E. López-Aguilar, S. M. Fielding, A. Frishman, M. D. Graham, J. S. Guasto, S. J. Haward, S. Hormozi, G. H. McKinley, R. J. Poole, A. Morozov, V. Shankar, E. S. G. Shaqfeh, A. Q. Shen, H. Stark, V. Steinberg, G. Subramanian, and H. A. Stone, "Perspectives on viscoelastic flow instabilities and elastic turbulence," arXiv:2108.09841 [physics.flu-dyn] (2021).
[49]A. M. Howe, A. Clarke, and D. Giernalczyk, "Flow of concentrated viscoelastic polymer solutions in porous media: Effect of mw and concentration on elastic turbulence onset in various geometries," Soft Matter **11**, 6419–6431 (2015).
[50]C. A. Browne and S. S. Datta, "Elastic turbulence generates anomalous flow resistance in porous media," arXiv:2011.06036 [physics.flu-dyn] (2020).
[51]D. Kawale, E. Marques, P. L. Zitha, M. T. Kreutzer, W. R. Rossen, and P. E. Boukany, "Elastic instabilities during the flow of hydrolyzed polyacrylamide solution in porous media: Effect of pore-shape and salt," Soft Matter **13**, 765–775 (2017).
[52]E. S. Shaqfeh, "Purely elastic instabilities in viscometric flows," Annu. Rev. Fluid Mech. **28**, 129–185 (1996).
[53]A. Clarke, A. M. Howe, J. Mitchell, J. Staniland, L. Hawkes, and K. Leeper, "Mechanism of anomalously increased oil displacement with aqueous viscoelastic polymer solutions," Soft Matter **11**, 3536–3541 (2015).
[54]J. Mitchell, K. Lyons, A. M. Howe, and A. Clarke, "Viscoelastic polymer flows and elastic turbulence in three-dimensional porous structures," Soft Matter **12**, 460–468 (2016).
[55]C. Xie, K. Xu, K. Mohanty, M. Wang, and M. T. Balhoff, "Nonwetting droplet oscillation and displacement by viscoelastic fluids," Phys. Rev. Fluids **5**, 063301 (2020).

[56]M. A. Nilsson, R. Kulkarni, L. Gerberich, R. Hammond, R. Singh, E. Baumhoff, and J. P. Rothstein, "Effect of fluid rheology on enhanced oil recovery in a microfluidic sandstone device," J. Non-Newtonian Fluid Mech. **202**, 112–119 (2013).
[57]S. De, P. Krishnan, J. van der Schaaf, J. Kuipers, E. Peters, and J. Padding, "Viscoelastic effects on residual oil distribution in flows through pillared microchannels," J. Colloid Interface Sci. **510**, 262–271 (2018).
[58]Y. Xia and G. M. Whitesides, "Soft lithography," Annu. Rev. Mater. Sci. **28**, 153–184 (1998).
[59]American Petroleum Institute, *Recommended Practices for Evaluation of Polymers Used in Enhanced Oil Recovery Operations* (American Petroleum Institute, 1990), Vol. 63.
[60]T. G. Mezger, *The Rheology Handbook: For Users of Rotational and Oscillatory Rheometers* (Vincentz Network GmbH & Co KG, 2006).
[61]A. V. Dobrynin, R. H. Colby, and M. Rubinstein, "Scaling theory of polyelectrolyte solutions," Macromolecules **28**, 1859–1871 (1995).
[62]C. W. Macosko, *Rheology: Principles, Measurements and Applications* (Wiley-VCH, 1994), Vol. 86.
[63]H. A. Barnes, J. F. Hutton, and K. Walters, *An Introduction to Rheology* (Elsevier, 1989), Vol. 3.
[64]T. Burghelea and V. Bertola, *Transport Phenomena in Complex Fluids* (Springer, 2020), Vol. 598.
[65]J. L. White and A. B. Metzner, "Development of constitutive equations for polymeric melts and solutions," J. Appl. Polym. Sci. **7**, 1867–1889 (1963).
[66]H. Bodiguel, J. Beaumont, A. Machado, L. Martinie, H. Kellay, and A. Colin, "Flow enhancement due to elastic turbulence in channel flows of shear thinning fluids," Phys. Rev. Lett. **114**, 028302 (2015).
[67]A. Soulies, J. Aubril, C. Castelain, and T. Burghelea, "Characterisation of elastic turbulence in a serpentine micro-channel," Phys. Fluids **29**, 083102 (2017).
[68]L. Casanellas, M. A. Alves, R. J. Poole, S. Lerouge, and A. Lindner, "The stabilizing effect of shear thinning on the onset of purely elastic instabilities in serpentine microflows," Soft Matter **12**, 6167–6175 (2016).
[69]ANSYS, *ANSYS Polyflow User's Guide* (ANSYS Inc., 2020).
[70]Y. Son, "Determination of shear viscosity and shear rate from pressure drop and flow rate relationship in a rectangular channel," Polymer **48**, 632–637 (2007).
[71]L. Ducloué, L. Casanellas, S. J. Haward, R. J. Poole, M. A. Alves, S. Lerouge, A. Q. Shen, and A. Lindner, "Secondary flows of viscoelastic fluids in serpentine microchannels," Microfluid. Nanofluid. **23**, 33 (2019).
[72]R. Poole, A. Lindner, and M. Alves, "Viscoelastic secondary flows in serpentine channels," J. Non-Newtonian Fluid Mech. **201**, 10–16 (2013).
[73]B. A. Schiamberg, L. T. Shereda, H. Hu, and R. G. Larson, "Transitional pathway to elastic turbulence in torsional, parallel-plate flow of a polymer solution," J. Fluid Mech. **554**, 191–216 (2006).